

MDPI

Article

Combustion Synthesis of Zirconium-Doped Ceria Nanocatalyst

Katarina Mužina 1,* , Stanislav Kurajica 1, Helena Bach-Rojecky 2 , Filip Brleković 1 and Marina Duplančić 3

- Faculty of Chemical Engineering and Technology, University of Zagreb, Marulićev trg 19, 10 000 Zagreb, Croatia; stankok@fkit.unizg.hr (S.K.); fbrlekovi@fkit.unizg.hr (F.B.)
- ² Ruđer Bošković Institute, Bijenička Cesta 54, 10 000 Zagreb, Croatia; helena.bach-rojecky@irb.hr
- ³ Croatian Accreditation Agency, Ulica Grada Vukovara 78, 10 000 Zagreb, Croatia; marina.duplancic@akreditacija.hr
- * Correspondence: kmuzina@fkit.unizg.hr

Abstract: Zirconium-doped ceria is a promising and extensively researched catalytic material with notable use in three-way catalytic converters, the oxidation of volatile organic compounds and solid oxide fuel cells. In this work, pure and zirconium-doped ceria nanoparticles ($Ce_{1-x}Zr_xO_2$, where x=0,0.1,0.2, and 0.3) were prepared by combustion synthesis using glycine as the fuel and cerium and zirconium nitrate as oxidants. The obtained powders were characterized using X-ray powder diffraction, scanning electron microscopy, Fourier transform infrared spectroscopy, differential thermal and thermogravimetric analysis, UV–Vis diffuse reflectance spectroscopy, and X-ray photoelectron spectroscopy. The combustion temperature increases with the increase in zirconium content in the samples, but the XRD patterns exclusively show ceria diffraction peaks. The crystallite sizes are in the range from 25.2 to 11.7 nm, and do not vary substantially after thermal treatment, indicating the good thermal stability of the prepared nanocatalysts. XPS analysis showed that the surface amount of zirconium is lower than the nominal and that the ceria sample with 10 mol. % of zirconium has a higher amount of oxygen vacancies than the 30 mol. % Zr-doped sample. The 10 mol. % Zr-doped sample displays the best catalytic activity in the BTEX (benzene, toluene, ethylbenzene, and o-xylene) oxidation process.

Keywords: ceria; nanocatalysts; combustion synthesis; solid solution; zirconium



Citation: Mužina, K.; Kurajica, S.; Bach-Rojecky, H.; Brleković, F.; Duplančić, M. Combustion Synthesis of Zirconium-Doped Ceria Nanocatalyst. *Crystals* **2024**, *14*, 108. https://doi.org/10.3390/ cryst14020108

Academic Editors: Kamila Komędera, Karolina Siedliska and Raffaello Mazzaro

Received: 24 December 2023 Revised: 17 January 2024 Accepted: 20 January 2024 Published: 23 January 2024



Copyright: © 2024 by the authors. Licensee MDPI, Basel, Switzerland. This article is an open access article distributed under the terms and conditions of the Creative Commons Attribution (CC BY) license (https://creativecommons.org/licenses/by/4.0/).

1. Introduction

Ceria (CeO₂) is an auspicious and widely applied catalytic material, owing to its oxygen storage and release capacity originating from the reversible redox reaction between Ce³⁺ and Ce⁴⁺ ions inside the ceria crystal lattice, as well as its thermal and mechanical stability and reasonable price. The physicochemical properties of ceria can be further improved by the introduction of defects, i.e., by replacing the cerium atom in the crystal lattice of ceria with an atom of different radius or valence, which is known as doping. The doping elements can be various transition or rare earth elements [1], among which zirconium stands out as one of the most common and most researched dopants [2,3]. Zirconiumdoped ceria (Ce_xZr_{1-x}O₂) solid solution shows improved oxygen mobility and oxygen storage capacity, better thermal stability, and enhanced catalytic activity [2]. Therefore, Zr-doped ceria has been extensively investigated for its application in supercapacitors [4], where it was proven that Zr doping enhances the pseudocapacitive behavior of ceria; in sensors [5]; as anticorrosion pigments in waterborne epoxy–polymer coatings [3]; and, most importantly, in catalysis [6–11]. Comprehensive reviews of the various possible catalytic applications of doped cerium oxide are given in the works of Trovarelli et al. [9,10] and Montini et al. [11]. The well-established catalytic uses of $Ce_xZr_{1-x}O_2$ are as a promoter in three-way catalytic converters for the removal of pollutants stemming from the incomplete combustion of gasoline in automobile engines and a catalyst for the oxidation of soot and reduction of NO_x in diesel engines [9,11]. Among the emerging catalytic applications, the

catalytic oxidation of volatile organic compounds presents an important area of research from the perspectives of environmental and human health protection [11,12]. Ceria is usually used in combination with noble metals or in the form of mixed oxides. In case of, e.g., methane, which is considered to be the most difficult to oxidize, pure ceria and mixed oxides, such as CeO₂-ZrO₂ systems, displayed satisfactory conversion in the medium to high temperature range, while the addition of noble metals shifted the conversion to lower temperatures [11]. However, the goal is to achieve high conversion at lower temperatures without the addition of noble metals or, at least, the addition of as little as possible. In other words, the final goal is to make the abatement of VOCs an energy efficient and low-cost process. Therefore, the choice of the correct catalyst, with a high specific surface area, good catalytic activity, and thermal and mechanical stability, is crucial. The desired properties can be achieved by choosing the right dopant, reducing the particle size to the nanoscopic scale, and tuning the morphology of the prepared catalyst, which is directly linked to the choice of the correct preparation method.

There are many available methods for the preparation of ceria nanoparticles, including hydrothermal and solvothermal synthesis, the sol-gel method, mechanochemical synthesis, precipitation method, spray pyrolysis, etc. [13]. Solution combustion synthesis (SCS) has become a very attractive method for the preparation of nanomaterials in the last few years because it involves a very simple and fast process that does not require complicated equipment or expensive chemicals. Essentially, SCS is a self-sustained reaction between oxidants (usually metal nitrates) and a fuel (such as urea, citric acid, different amino acids, etc.), which are dissolved in water to form a saturated solution and heated until all the water evaporates and the mixture self-ignites. This method enables the preparation of nanosized metal oxide materials, often without the need for subsequent thermal treatment; a uniform addition of small amounts of the doping agent; and a good control of the reaction parameters, mainly through the fuel to oxidant ratio (F/O), which has a significant effect on the properties (crystallite size, morphology, specific surface area, etc.) of the final product [14]. The fuel to oxidant ratio is established by balancing reducing elements, with valences that are considered positive, and oxidizing elements with negative valences. The fuel and the oxidant both consist of oxidizing and reducing elements, which is why the fuel to oxidant ratio is conveyed by elemental stoichiometric coefficients as the equivalence ratio (φ), defined by the following equation:

$$\varphi = \frac{n_{\text{fuel}} \sum \text{stoichiometric coefficient} \times \text{valence}}{-n_{\text{oxidant}} \sum \text{stoichiometric coefficient} \times \text{valence}}$$
(1)

where $n_{\rm fuel}$ is the molar fraction of the chosen fuel and $n_{\rm oxidant}$ is the molar fraction of metal salts used as oxidants. Metal cations, carbon, and hydrogen are regarded as reducing elements with their respective valences, oxygen as an oxidizing element with a valence of -2, and nitrogen as a neutral element with zero valence. When the equivalence ratio is equal to 1, the mixture is stoichiometric and maximal energy is released; when it is <1, the mixture is fuel lean; and when $\varphi > 1$, the mixture is fuel rich [15].

Even though zirconium-doped ceria is not a novel material, but rather a well-researched and valuable catalyst, the improvement of its properties in order to match various applications is of utmost importance. Our group has perfected the combustion synthesis of extremely porous and catalytically active nanomaterials, as well as catalyst supports using glycine as the fuel and metal nitrates as oxidants [15,16]. Additionally, extensive work has examined ceria-based nanocatalysts doped with various transition metals and prepared by different synthesis methods, aimed at the oxidation of volatile organic compounds [17,18]. The present work is the result of this combined knowledge and is a thorough study of nanocrystalline ceria catalysts doped with 10, 20, and 30 mol. % of zirconium prepared by a simple and affordable solution combustion synthesis method. The prepared nanocatalysts, as well as samples thermally treated at 500 °C for 2 h, are characterized by various techniques. Their catalytic activity is tested on the benzene, toluene, ethylbenzene, and

Crystals **2024**, 14, 108 3 of 16

o-xylene (BTEX) oxidation process. The results of this study provide new insights into the morphology, thermal stability, and catalytic activity of zirconium-doped ceria nanocatalysts.

2. Materials and Methods

2.1. Synthesis

Pure ceria sample and ceria samples doped with 10, 20, and 30 mol. % of zirconium, denoted CeO₂, 10Zr:CeO₂, 20Zr:CeO₂, and 30Zr:CeO₂, respectively, were prepared using combustion synthesis with cerium nitrate hexahydrate, Ce(NO₃)₃·6H₂O (p.a., Acros Organics, Geel, Belgium) and zirconium oxynitrate n-hydrate, ZrO(NO₃)₂·nH₂O (p.a., Merck, Germany) as oxidants, and glycine (p.a., Lachner, Neratovice, Czech Republic) as fuel. The appropriate amounts of precursors were calculated based on equation 1 and placed in a porcelain bowl with 10 mL of demineralized water. The aqueous mixture of precursors was stirred at 300 rpm and 60 °C until the water evaporated and a viscous sludge remained. The mixture was then relocated into a sand bath inside a fume hood; the temperature of the sand bath was set to maximum (700 °C) and the temperature of the reaction mixture was monitored with an IR pyrometer. After the combustion reaction, evidenced by an intense yellow flame and the release of a large amount of gases, a fine yellow powder product of low density remained. The yellow color became brighter as the amount of added zirconium increases. The as-prepared samples were thermally treated at 500 °C for 2 h in order to gain insight in the thermal stability of the samples and potential crystallization of impurities or zirconium-based phases, as well as to prepare them for the catalytic activity test, since 500 °C is the maximum temperature expected to be reached during the tests, based on our previous research regarding VOCs oxidation with the use of ceria-based nanocatalysts [18].

2.2. Characterization

The phase composition was determined by X-ray diffraction analysis (XRD) on a Shimadzu XRD 6000 (Shimadzu, Tokyo, Japan) with CuK α irradiation, accelerating voltage of 40 kV, and current of 30 mA. The XRD patterns were obtained in step scan mode in the range between 10 and 105° 20, with 0.02° 20 step and retention time of 0.6 s. The crystallite size was calculated using the Scherrer equation based on the Bragg angle of the (220) ceria diffraction peak, as described in reference [17]. The unit cell constant (a) of ceria cubic structure was determined using the UnitCell program.

Fourier transform infrared spectroscopy (FTIR) was applied with the aim of identifying phases and precursor residues that are not visible by XRD analysis. IR spectra were obtained using the Bruker Vertex 70 FTIR spectrometer (Bruker Optics, Karlsruhe, Germany) in attenuated total reflectance (ATR) mode in the range 4000– $400 \, \mathrm{cm}^{-1}$ with spectral resolution of 2 cm $^{-1}$ and an average of 32 scans.

Simultaneous differential thermal and thermogravimetric analyses (DTA-TGA) were performed on a NETZSCH STA 409C thermal analyzer (Netzsch-Gerätebau GmbH, Selb, Germany) by placing ~10 mg of the sample in a corundum crucible and heating it to 1000 °C with a heating rate of 10 °C min $^{-1}$ in a synthetic air flow of 30 cm 3 min $^{-1}$. Corundum was used as a reference.

UV–Vis reflectance spectra (UV-Vis DRS) used for the determination of band gap values of prepared samples were acquired using an Ocean Insight QE Pro High-Performance Spectrometer (Ocean Insight, Orlando, FL, USA)equipped with an integrating sphere for reflectance. The Kubelka–Munk function, F(R), was calculated based on the obtained spectra and further used in Tauc's plot, $[F(R)hv]^{1/2}$ vs. photon energy (hv), where ½ indicates the indirect band gap, h is Planck's constant, and v represents the light frequency [19]. The band gap values were determined by extrapolating the linear region of the attained curves onto the abscissa.

The insight into morphology and elemental composition of the prepared samples was obtained using the scanning electron microscope (SEM) Tescan Vega 3 Easyprobe (Tescan, Brno, Czech Republic) with accelerating voltage of 10 kV equipped with an energy dispersive X-ray spectroscopy (EDS) detector Bruker B-Quantax. Prior to analysis, the

Crystals **2024**, 14, 108 4 of 16

samples were fixed onto aluminum sample holders with double-sided carbon conductive tape and coated with gold and palladium using Quorum SC 7620 sputter coater.

X-ray photoelectron spectroscopy (XPS) performed on a SPECS spectrometer (Specsgroup, Berlin, Germany) equipped with an Al monochromatized X-ray source emitting at 1486.74 eV (AlK α line) and a Phoibos MCD 100 electron analyzer was used to determine the amounts of zirconium, cerium, and oxygen ions in the samples along with their oxidation states. Mixed Gaussian–Lorentzian functions with Shirley background subtraction were applied for the deconvolution of experimental curves in Fityk 1.3.1 software.

Physisorption data were acquired on a Micromeritics ASAP-2000 instrument (Micromeritics, Atlanta, GA, USA) at 77 K. The samples were degassed at 100 °C in a dynamic vacuum of 7 mPa before the analysis to remove potential surface-adsorbed species. The Barrett–Joyner–Halenda (BJH) method was used to calculate the pore size, while the specific surface area was determined by the Brunauer–Emmett–Teller (BET) method.

The catalytic activity tests were performed in an integral up-flow fixed bed reactor (I.D: 7 mm) at atmospheric pressure. A gas mixture of benzene, toluene, ethylbenzene, and o-xylene (BTEX) in nitrogen (52.1 ppm of benzene, 52.4 ppm of toluene, 49.9 ppm of ethylbenzene, and 55.4 ppm of o-xylene in nitrogen, Messer Croatia Plin d.o.o., Zaprešic, Croatia) with a gas flow rate of 12 cm 3 min $^{-1}$ was used for model VOCs for the catalytic oxidation process. First, 50 mg of the nanocatalyst powder was placed inside the reactor between two quartz wool plugs with inert quartz inserts, which serve to preheat the gas mixture before it enters the catalyst layer. The gas flow rates were adjusted by mass flow controllers (MFC 4800 Series, Brooks, Hatfield, PA, USA), while the reactor temperature was regulated by a thermo-controller (TC208 Series). An on-line gas chromatograph (GC-2014, Shimadzu, Tokyo, Japan) with a flame ionization detector (FID) and an RTX-WAX column (1 µm) was employed for ascertaining the BTEX concentration in the reactor.

3. Results and Discussion

As was mentioned, the reaction mixture temperature was monitored with an IR pyrometer and the results are shown in Figure 1. When the temperature is high enough to initiate a spontaneous combustion reaction, an intense increase in temperature can be observed. It can also be seen that the maximum temperature of the combustion process increases with an increase in the amount of zirconium doping, and the highest combustion temperature (896 °C) is recorded for the reaction mixture containing 30 mol. % Zr. The reaction is highly exothermic and very fast, as evidenced by the sudden drop in temperature after the maximum is reached, which signifies the completion of the reaction. Oscillations in the temperature before the start of the combustion reaction are caused by directing the targeting beam of the IR pyrometer at the bubbles that are formed during the heating of the reaction mixture. Regarding the ignition time, it is not possible to observe a trend because the ignition depends on the amount of residual water at the moment when the mixing is stopped, the reaction mixture transferred to the sand bath, the position of the porcelain bowl in the sand bath, and the configuration of the foil with which the container is covered in order to prevent excessive sample loss. The synthesis of the pure ceria sample seemed the most violent, with an intense flame, even though the maximum temperature was the smallest, and the final product consisted of yellow, light, and porous flakes that were crushed into powder. The combustion reactions of zirconium-doped samples were less intense, but the final product was similar in appearance, except for the sample 30Zr:CeO₂, which consisted of light-yellow sheets.

Crystals **2024**, 14, 108 5 of 16

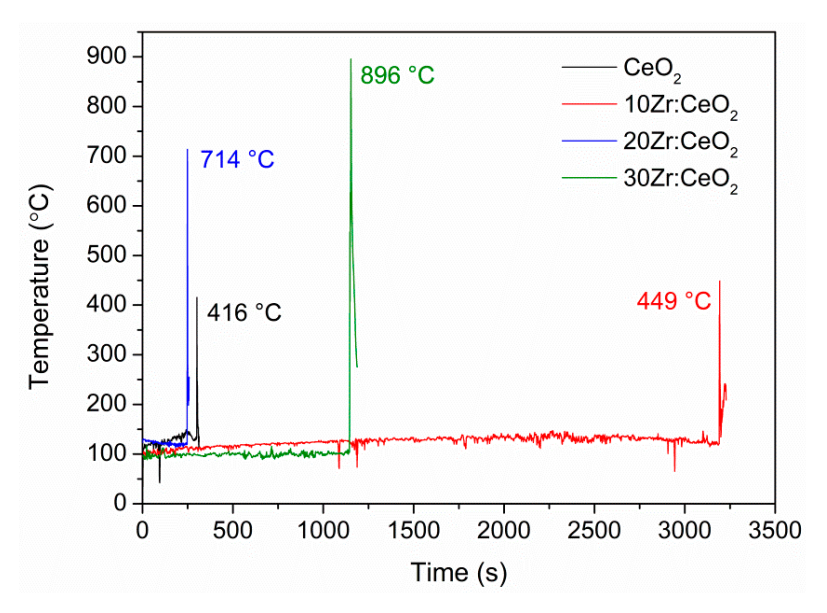


Figure 1. Temperature vs. time curves for all samples.

Due to the extreme similarity of XRD patterns of as-prepared and thermally treated samples, only XRD patterns of thermally treated samples are shown in Figure 2a. It can be seen that they consist solely of ceria diffraction peaks (ICDD PDF-2 34-0394). No zirconium-based phases are visible, even at the highest doping amount, neither for the as-prepared nor thermally treated samples, indicating that zirconium is incorporated into the ceria crystal lattice, forming a solid solution. The crystallite sizes listed in Table 1 show a clear decreasing trend with increasing zirconium doping amount, signifying a positive influence of zirconium on this property of ceria nanocatalysts. The reduction in crystallite size is particularly pronounced when comparing the undoped ceria sample with the 10 mol. % Zr-doped sample, while the differences between the doped samples are much smaller. This indicates that the increase in Zr amount after 10 mol. % does not dramatically affect the crystallite size.

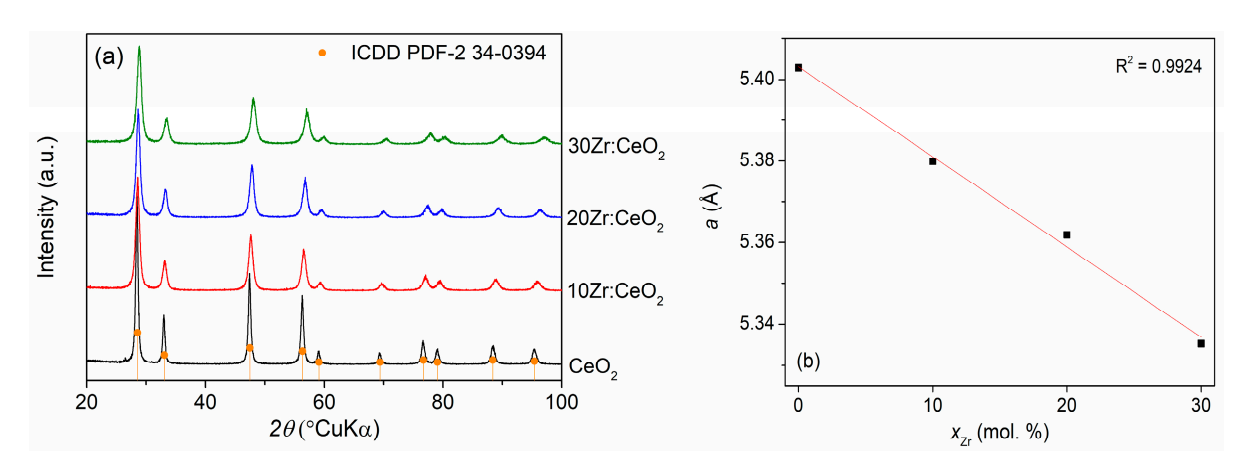


Figure 2. XRD patterns of all thermally treated samples (**a**) and the dependence of the unit cell constant *a* on the Zr doping amount (**b**).

Crystals **2024**, 14, 108 6 of 16

Table 1. Crystallite sizes (L) and band gap values (E_g) of as-prepared samples, as well as crystallite sizes ($L_{500^{\circ}\text{C}/2\text{h}}$), unit cell constants (a), specific surface areas (S_{BET}), average pore diameters, and cumulative adsorption pore volumes of thermally treated samples.

	CeO ₂	10Zr:CeO ₂	20Zr:CeO ₂	30Zr:CeO ₂
L, nm	25.2 ± 0.9	13.7 ± 0.3	12.4 ± 0.3	11.7 ± 0.3
$E_{\rm g}$, eV	2.59	2.62	2.52	2.43
$E_{ m g}$, eV $L_{ m 500^{\circ}C/2h}$, nm a , Å	30.5 ± 1.2	14.2 ± 0.4	14.3 ± 0.4	11.4 ± 0.3
a, Å	5.40 ± 0.0001	5.38 ± 0.0001	5.36 ± 0.0001	5.34 ± 0.0001
$S_{ m BET}$, m ² g ⁻¹	30.1	36.8	36.6	29.3
Average pore diameter, nm	10.9	11.4	12.3	13.1
Cumulative adsorption pore volume, $cm^3 g^{-1}$	0.092	0.134	0.125	0.110

Another occurrence observed on the XRD patterns is a small but noticeable shift in the peaks to higher angles with the increase in the zirconium doping amount, which indicates a change in unit cell constant values with the addition of zirconium. Figure 2b shows the dependence of the unit cell constant (a) of ceria cubic crystal structure, calculated based on the fitting results of all obtained peaks in the XRD spectra, on the zirconium doping amount. An almost-perfect linear dependence indicates that the obtained samples abide by Vegard's law, an empirical rule according to which the unit cell constant of a solid solution of two components is approximately equal to the weight average of the unit cell constants of the specified components at the same temperature [20]. This is a proof of a solid solution formation, or more precisely, of substitutional doping of Zr in the ceria crystal lattice, since the replacement of larger Ce⁴⁺ (97 pm) with smaller Zr⁴⁺ (84 pm) is expected to cause a reduction in the crystal lattice [7].

The crystallite sizes of thermally treated samples are very similar to the as-prepared samples, pointing out the positive influence of zirconium on ceria thermal stability. This is especially true for the 30 mol. % Zr-doped sample, for which the crystallite size, when including the error of the Scherrer method, stays practically the same after thermal treatment. The thermal stability of a catalyst is a very important factor in catalytic processes, because it directly affects its catalytic activity and specific surface area; thus, these results are very auspicious.

The FTIR spectroscopy results of as-prepared samples displayed in Figure 3 show bands corresponding to vibrations in metal–oxygen bonds present in all samples in the fingerprint region to 600 cm⁻¹. The bands between 1300 and 1700 cm⁻¹ encompass the bands for nitrate residues, as well as glycine and organic residues, indicating that the reaction is not complete, i.e., that there are remnants of precursors and combustion products present in the samples. However, these bands are not pronounced, but rather broad and faint, which suggests that these remnants are present in a small amount. The indistinct band at around 2300 cm⁻¹ belongs to carbon dioxide adsorbed on the surface of the samples, while the faint, broad band between 3200 and 3700 cm⁻¹ is characteristic of the stretching of O-H bonds in water molecules [21,22]. Samples obtained through combustion synthesis usually have considerable specific surface area, so the presence of adsorbed species, such as water and carbon dioxide, is quite common. The FTIR spectra of thermally treated samples (not shown in this paper) are quite similar to the as-prepared samples, but with decreased intensity of nitrate, organic, and water-related bands, which is to be expected as a consequence of thermal treatment.

Crystals **2024**, 14, 108 7 of 16

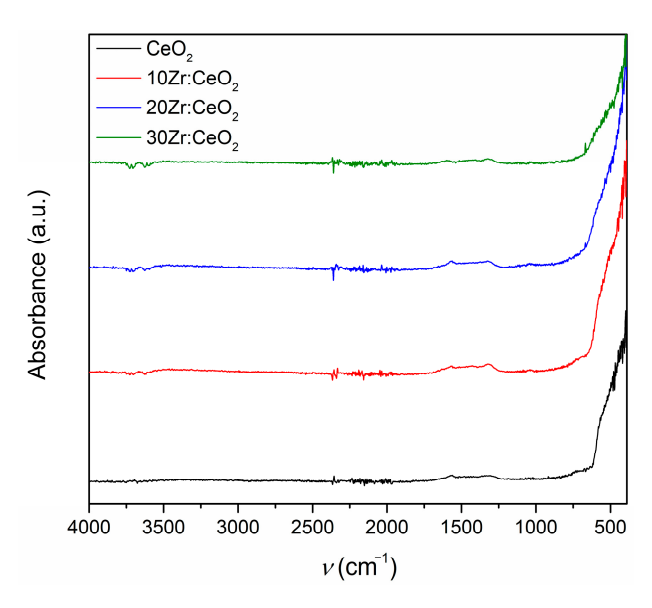


Figure 3. FTIR spectra all as-prepared samples.

Differential thermal and thermogravimetric analyses were performed to shed light on thermal properties and stability of prepared samples. The results are presented in Figure 4a,b. The pure ceria sample and $20Zr:CeO_2$ sample show the largest total mass losses, of ~2.85%. The $10Zr:CeO_2$ exhibits a slightly smaller total mass loss of 2%, while the sample $30Zr:CeO_2$ exhibits a small mass loss (~0.37%) below 100 °C, which is followed by continuous mass gain (~2.25%) to 1000 °C. A small mass loss below 100 °C, present in all samples (Figure 4a) and followed by a small endothermic peak on the DTA curve (Figure 4b), corresponds to the loss of water and other volatile adsorbed species [23–25]. All samples except $30Zr:CeO_2$ show the greatest mass loss in the range between 150 and 350 °C, after which the mass remains unchanged. The pure ceria sample shows two exothermic peaks in this region centred at ~170 and ~274 °C, while 10 and 20 mol. % Zr-doped samples display only one peak at ~310 °C. According to literature [24], this mass loss can be attributed to the decomposition of organic matter, the decomposition of reactants that did not react during combustion synthesis, and the burning of gaseous decomposition products.

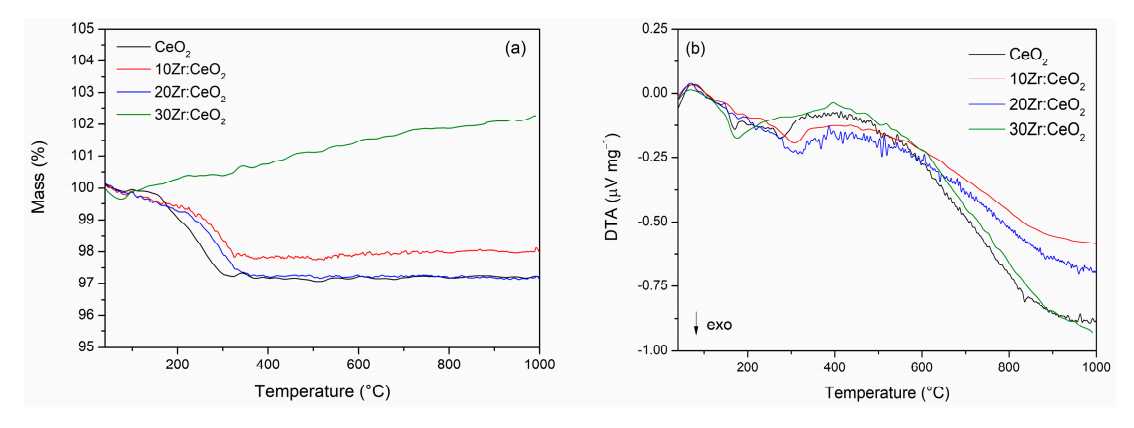


Figure 4. TGA curves (a) and DTA curves (b) of all as-prepared samples.

The 30 mol. % Zr-doped ceria sample differs from pure and other doped samples. Namely, the combustion process of that sample was the least intense and resembled smouldering rather than burning. A powder of extremely low density was also obtained, and the very morphology of that sample is different compared to the others, as will be shown below. The preparation of the 30Zr:CeO₂ sample for thermal analysis was a problem precisely due to the low density, and the sample had to be well pressed into the crucible so

that it would not fly out during the analysis. Mass increase during DTA-TGA analysis in the air atmosphere is most often a consequence of an oxidation process; however, in this case, the only possible process is the oxidation of Ce³⁺ to Ce⁴⁺, and the XPS analysis shows that the sample with 10 mol. % Zr has more Ce³⁺ ions on the surface and still does not show an increase in mass. Therefore, a different explanation had to be sought. Repeated analyses showed that the more the sample is pressed into the crucible, the smaller the increase in mass, which indicates that the mass gain is most likely a consequence of buoyancy. When gas is introduced into the chamber, the sample experiences a buoyant lift according to Archimedes' principle. As the temperature rises, the gas becomes less dense, making the buoyant lift less pronounced, and the sample starts moving downward, which is registered as weight gain [26].

SEM images of all as-prepared samples are shown in Figure 5. It can be observed that the samples CeO_2 , $10Zr:CeO_2$, and $20Zr:CeO_2$ contain particle agglomerates with a sea-wave foam-like, extremely porous morphology. Sample $30Zr:CeO_2$ also exhibits a porous morphology, but with sponge-like particle agglomerates. The porous microstructure is caused by the formation of gases during the synthesis.

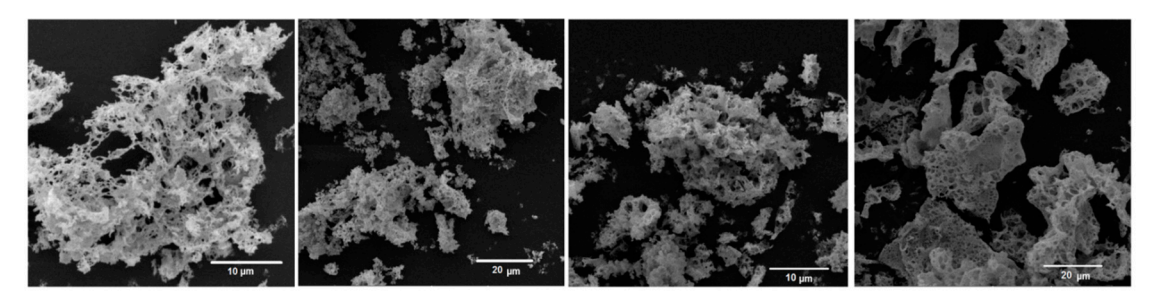


Figure 5. SEM images of all as-prepared samples (from left to right: CeO_2 , $10Zr:CeO_2$, $20Zr:CeO_2$, and $30Zr:CeO_2$).

Figure 6 shows the distribution of individual elements in the zirconium-doped asprepared samples, as well as sample $30Zr:CeO_2$ that was thermally treated at $500\,^{\circ}C$ for 2 h. The distribution of Ce, O, and Zr ions is mostly homogeneous throughout the samples, especially taking into account the porosity of the samples, which makes the EDS map appear disordered. It can also be observed that the amount of Zr increases with the increase in the nominal amount.

The UV-Vis DRS spectra (Figure 7) show that all samples exhibit high reflectance in the visible region, a decrease in reflectance at the transition from the visible to the UV region, and high absorbance in the UV region. It can be seen that the reflectance values in the visible region exceed 100%, which should be impossible. There are several possible reasons: contamination of the standard, a too-smooth sample surface resulting in a noticeable proportion of specular reflection, and the fact that cerium is a lanthanide that can exhibit luminescence. In our case, the latter two reasons are the most likely.

Even though ceria is usually considered a direct semiconductor, the Tauc plot for direct transitions did not result in a linear region that could enable a valid determination of the band gap. Therefore, only indirect band gap values obtained from the Tauc plot are listed in Table 1. The band gap value listed in the literature for both direct and indirect transitions is ~ 3.19 eV for bulk ceria and is slightly increased in the case of CeO_2 nanoparticles due to the quantum confinement effect [27,28]. The band gap values of all samples in this work are much smaller than the literature value (Table 1): the band gaps of pure and 10 mol. % Zr-doped CeO_2 are very similar, and then a decline is observed with an increase in zirconium doping amount. The redshift instead of a blueshift in the band gap of pure ceria nanoparticles is most likely the consequence of Ce^{3+} ions on the surface of the nanoparticles, as well as oxygen defects, which instil defect energy states between the valence and the conduction band [29,30]. In case of zirconium-doped samples, a decrease in band gap with an increase in zirconium doping is often reported in the literature and explained by the

Crystals **2024**, 14, 108 9 of 16

hybridization of empty Zr4d orbital with the Ce4f orbital, which results in a broadening of the conduction band and a narrowing of the band gap [2,7,31]. Nevertheless, the band gap values of zirconium-doped ceria samples are unprecedentedly small, which is beneficial for a potential use in photocatalysis since visible light could be used for excitation. However, the activity of a photocatalyst depends on multiple factors, which is why further experiments are necessary to assess their suitability for photocatalytic application.

XPS analysis was performed on two representative samples ($10Zr:CeO_2$ and $30Zr:CeO_2$) with the aim of determining the relative abundance of the elements on the surface of the samples, their chemical states, and surface oxygen species. The Ce 3d spectra of both samples with assigned deconvoluted peaks are displayed on Figure 8. The spectra show the presence of cerium in two oxidation states: the peaks denoted as v_0 , v', u_0 , and u' belong to the Ce^{3+} ion, while the peaks marked as v_0 , v'', v''', v''', v''', and u''' are associated with Ce^{4+} . The letters u and v designate the spin–orbit coupling $3d_{3/2}$ and $3d_{5/2}$, respectively [32]. The intensity of Ce^{3+} peaks is higher in the $10Zr:CeO_2$ spectrum, which is reflected in the Ce^{3+} and Ce^{4+} shares calculated from the deconvoluted peaks areas (Table 2). As can be seen in Table 2, the Ce^{3+} share in the sample with 10 mol. % Zr is twice as high as the share of the same ion in the sample with 30 mol. % Zr. This complements the DTA-TGA results well, because the final mass gain in the $10Zr:CeO_2$ can be assigned to the oxidation of Ce^{3+} into Ce^{4+} .

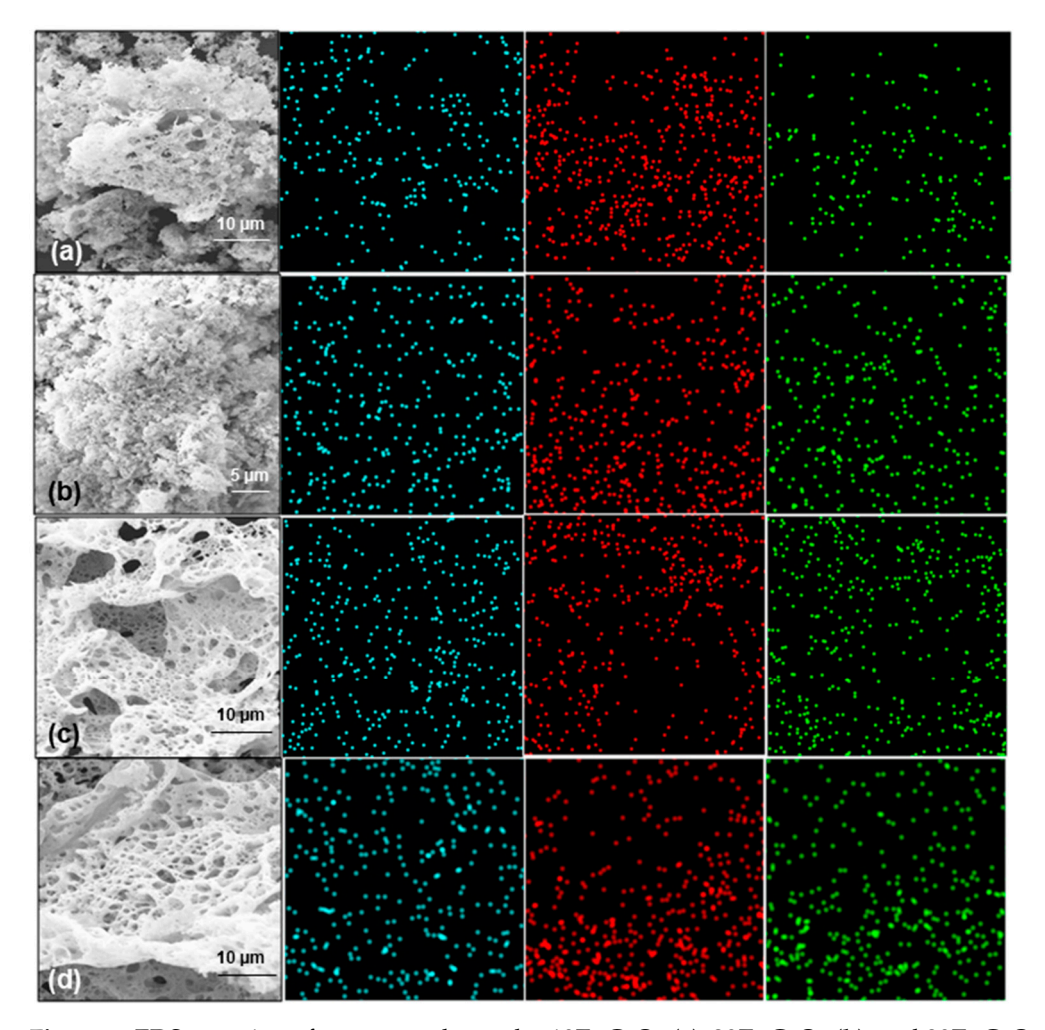


Figure 6. EDS mapping of as-prepared samples $10Zr:CeO_2$ (a), $20Zr:CeO_2$ (b), and $30Zr:CeO_2$ (c), as well as sample $30Zr:CeO_2$ thermally treated at 500 °C for 2 h (d). Cyan represents cerium, red represents oxygen, and green represents zirconium.

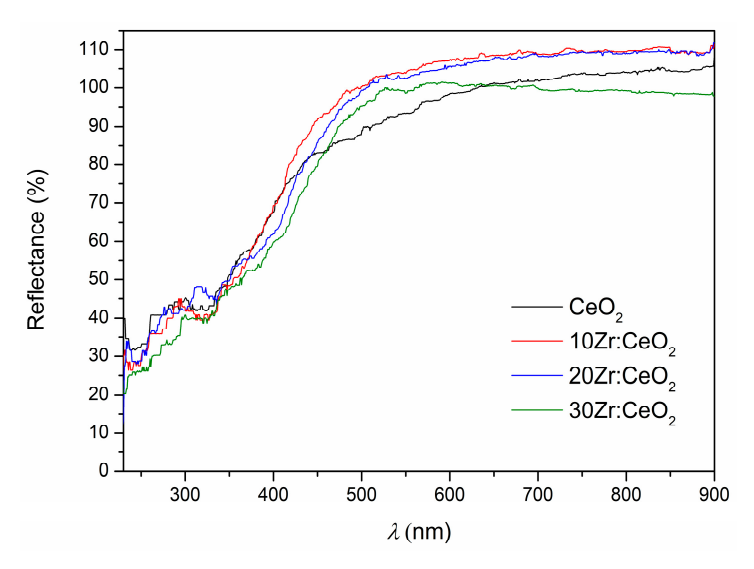


Figure 7. UV–Vis DRS spectra of all as-prepared samples.

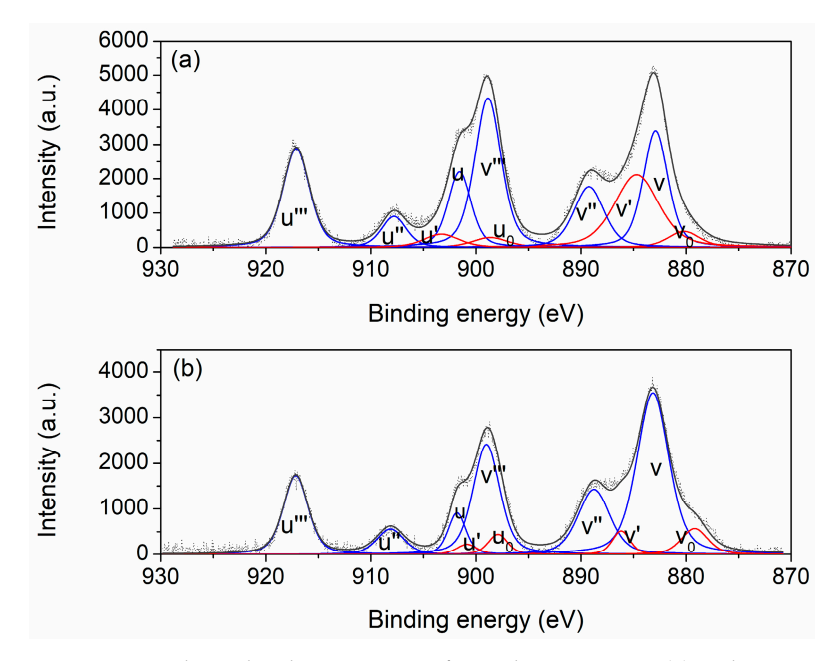


Figure 8. Ce 3d core level XPS spectra of samples $10Zr:CeO_2$ (a) and $30Zr:CeO_2$ (b). The black curves represent the full Ce 3d spectra, the blue curves represent the peaks associated with the Ce^{4+} ion, while the red curves represent the peaks corresponding to the Ce^{3+} ion.

Table 2. Molar fractions of cerium, oxygen, and zirconium at the surface of investigated as-prepared samples, as determined from XPS spectra.

	10Zr:CeO ₂	30Zr:CeO ₂
Ce ³⁺ (mol. %)	24.5	11.2
Ce ⁴⁺ (mol. %)	75.5	88.8
Lattice oxygen (mol. %)	89.9	93.6
Low coordination oxygen (mol. %)	11.1	6.4
Zr (mol. %)	3.9	13.0

The O 1s XPS spectra of the analyzed samples are shown in Figure 9. Two peaks can be observed on the spectra of both samples: the first, main peak at 530 eV and the second, shoulder peak at 533 eV. The main peak is assigned to ceria lattice oxygen, while the

shoulder is attributed to low coordination oxygen, i.e., oxygen adsorbed on the surface or present in surface hydroxyl groups or carbonate species, as well as oxygen ions in the oxygen-deficient regions near oxygen vacancies [33–35]. The intensity of both peaks is again higher for the 10 mol. % Zr-doped ceria sample. The higher share of low coordination oxygen, as given in Table 2 and calculated from respective peak areas, indicates a higher share of oxygen defects in this sample, which is beneficial from the point of view of potential catalytic applications.

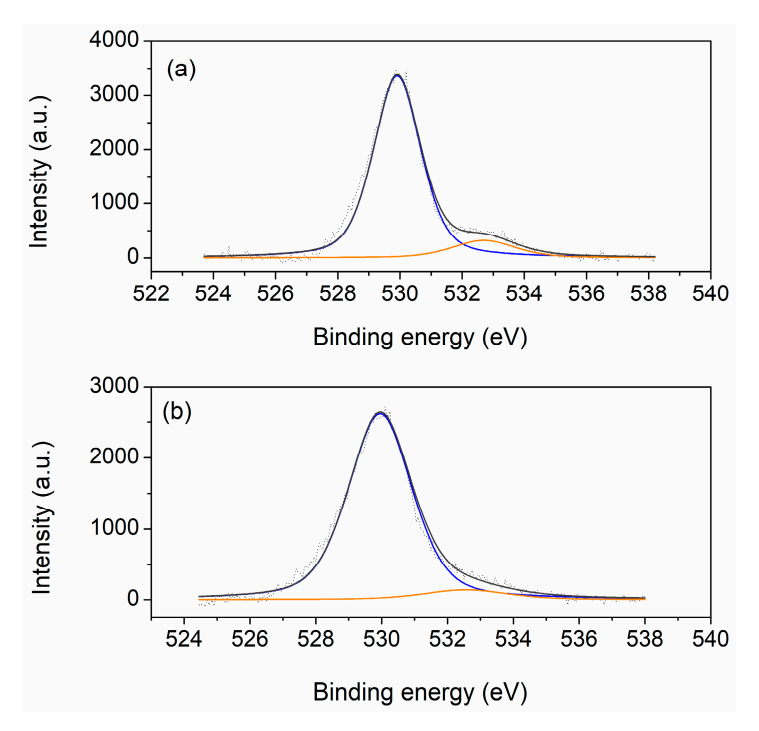


Figure 9. O 1s core level XPS spectra of samples $10Zr:CeO_2$ (a) and $30Zr:CeO_2$ (b). The black curves represent the full O 1s spectra, the blue curves represent the peaks associated with ceria lattice oxygen, while the orange curves represent the peaks corresponding to low coordination oxygen.

The Zr 3d spectra are presented in Figure 10. Two peaks can be observed for both samples: the first at \sim 182 eV and the second at \sim 184.5 eV, which correspond to Zr $3d_{5/2}$ and $Zr 3d_{3/2}$, respectively [36]. Both peaks are attributed to Zr^{4+} ions. The amount of zirconium on surface of the samples (Table 2) is lower than nominal and amounts to about 40% of the nominal share for both analyzed samples. Such a discrepancy between the nominal and actual amount of Zr on the surface of the samples is proposed by Koleva et al. [37] to be the consequence of the preference of zirconium ions to elude surface positions in ceria systems. This can originate from the difference in the ionic radius of Ce⁴⁺ and Zr⁴⁺ cations. The smaller Zr⁴⁺ ions tend to avoid the outer layer of ceria nanoparticles and instead occupy inner positions in a manner similar to smaller metal atoms preferring internal positions in bimetallic alloys. Additionally, the smaller ionic radius of the zirconium cation results in a stronger electrostatic field around it, so the zirconium cations are preferentially located inside where they can be better saturated, while the cerium ions with a weaker electrostatic field prevail at the surface where they are less surrounded by oxygen ions [37]. A similar effect arising from the difference in ionic radius was observed by Vari et al. in their study on the growth of cobalt on an ultrathin CeO₂(111) film; the results of the XPS analysis show that the diffusion of smaller Co²⁺ ions into the ceria lattice occurs, and that it is even more pronounced at higher temperatures [38].

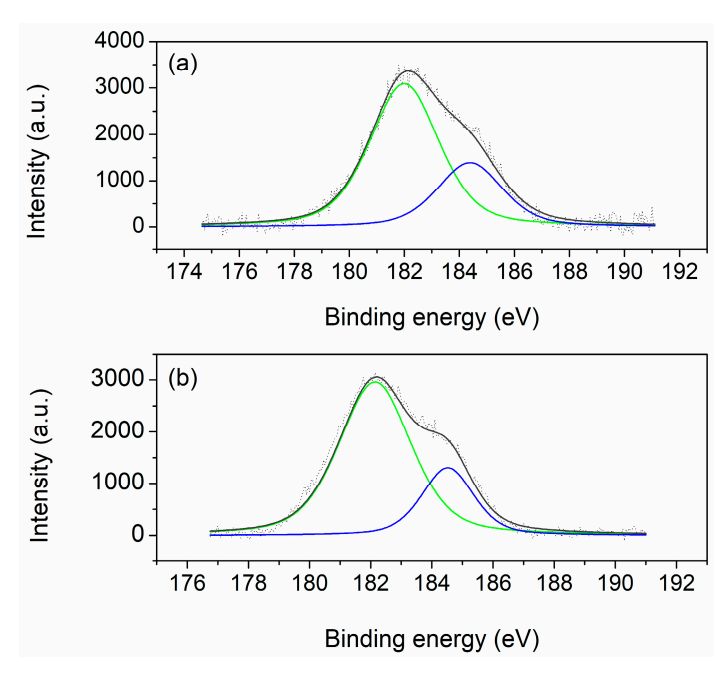


Figure 10. Zr 3d core level XPS spectra of samples 10Zr:CeO_2 (**a**) and 30Zr:CeO_2 (**b**). The black curves represent the full Zr 3d spectra, the blue curves represent the peaks associated with Zr $3d_{3/2}$, while the green curves represent the peaks corresponding to Zr $3d_{5/2}$.

The nitrogen adsorption–desorption isotherms of all thermally treated samples are displayed in Figure 11. According to IUPAC classification, the isotherms of all samples belong to type IV with H3 hysteresis loops, which are usually associated with mesoporous materials with pore sizes between 2 and 50 nm, implying the formation of particulate aggregates [39,40]. The average pore sizes listed in Table 1 confirm that these are indeed mesoporous materials. The average pore diameter increases with an increase in the amount of the zirconium doping. Conversely, the specific surface area values do not follow a particular trend, but can rather be divided into two groups: samples CeO₂ and 30Zr:CeO₂ have similar, smaller S_{BET} values around 30.0 m² g⁻¹, while samples 10Zr:CeO₂ and 20Zr:CeO₂ have higher specific surface areas around 36.7 m² g⁻¹. The specific surface area values are in the typical range for metal oxides prepared by solution combustion synthesis [41]. The cumulative pore volumes listed in Table 1 might serve as an explanation to the unusual grouping of the samples regarding S_{BET} values. The cumulative pore volumes for samples 10Zr:CeO₂ and 20Zr:CeO₂ are noticeably higher than for samples CeO₂ and 30Zr:CeO₂, indicating a higher porosity of these samples, which results in a higher specific surface area. In turn, higher specific surface area signifies that there are more catalytically active sites available for reaction, so the catalytic activity of these samples should be higher [42].

The thermally treated catalysts were tested in the process of the catalytic oxidation of VOCs. The mixture of benzene, toluene, ethylbenzene, and *o*-xylene was chosen as a model of VOCs. The reaction was carried out up to a temperature of 400 °C. The temperatures corresponding to 90% conversion for each of the samples and volatile organic compounds are shown in Figure 12. The 10Zr:CeO₂ sample is undoubtedly the most catalytically active, achieving 90% conversion of all volatile organic compounds at the lowest temperatures. It is followed by the 20Zr:CeO₂ sample, which also achieves the conversion of all analyzed compounds, but at higher temperatures. In the case of the undoped and 30 mol. % Zr-doped sample, 90% conversion of benzene could not be achieved in the studied temperature range. The undoped sample reaches 86% conversion at 400 °C, while the 30 mol. % Zr-doped sample barely reaches 40% conversion at the same temperature. Furthermore, the 30Zr:CeO₂ sample shows the lowest catalytic activity in the BTEX oxidation process, requiring significantly higher 90% conversion temperatures

than for any other sample. As for the conversion of individual volatile organic compounds, the catalytic activity of the studied catalysts increases in the order of benzene < toluene < ethylbenzene < o-xylene, which can be attributed to the decreasing stability of the benzene ring with the addition of substituents. Namely, the benzene ring is very difficult to oxidize due to its high symmetry and stability. The addition of substituents like methyl and ethyl groups has a considerable influence on the π electronic structure, as well as charge density distribution, thereby disrupting the aforementioned stability and symmetry, and facilitating the oxidation of such molecules at lower temperatures [43]. The oxidation of volatile organic compounds is a complex process, with various possible intermediate phases, and would require measurements of the concentration of possible products in the output stream. Unfortunately, our system can only measure the concentration of the reactants in the output stream, so further discussion on this matter is futile. However, what can be discussed is the properties of the prepared catalysts in regards to their catalytic activity. The catalytic activity of a catalyst depends on multiple factors, such as its structure, chemical composition, specific surface area, porosity, presence of defects, etc. [44]. Throughout this investigation, the 10Zr:CeO₂ sample has shown the most promising characteristics of a good catalyst: small crystallite size, good thermal stability, largest specific surface area, porous morphology, high share of Ce³⁺ ions, and low coordination oxygen indicating the presence of oxygen vacancies, which indeed resulted in the best catalytic activity among all of the prepared catalysts. Ramos-Fernandez et al. studied the CO₂ reduction process on doped cerium oxide as a catalyst, and they found out that CeO₂ doped with 10 mol. % of Zr has a higher rate of oxygen release due to the lower activation energy of this process (162 kJ mol⁻¹) compared to pure CeO_2 (235 kJ mol⁻¹) [45]. However, it would seem that a nominal Zr doping amount higher than 10 mol. % results in the gradual decrease in catalytic activity, meaning that 10 mol. % is the optimal zirconium doping amount.

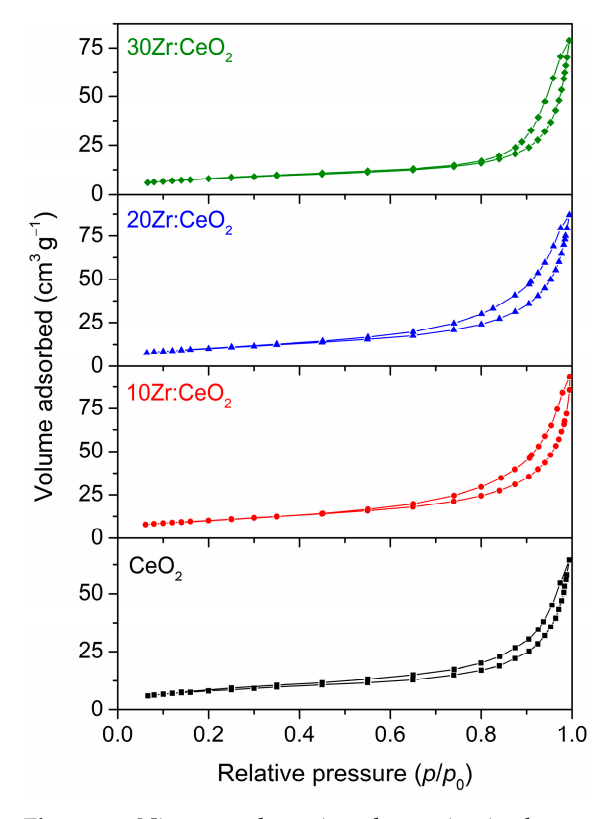


Figure 11. Nitrogen adsorption–desorption isotherms of all thermally treated samples.

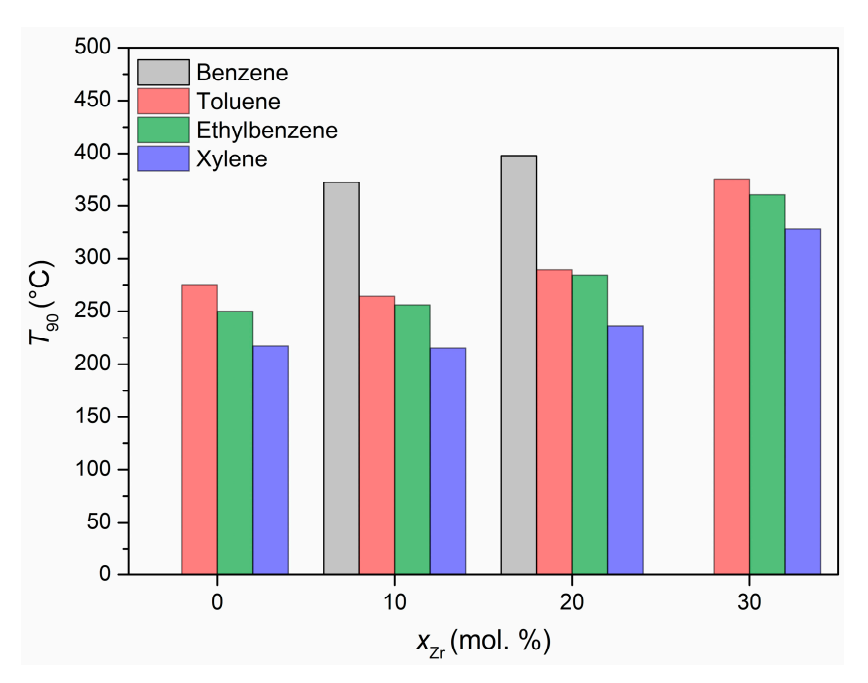


Figure 12. Temperature of 90% conversion vs. zirconium doping amount.

4. Conclusions

Pure and zirconium-doped ceria samples were prepared using the simple, energy efficient solution combustion synthesis method. The prepared samples were crystalline with extremely porous morphology. The XRD, EDS, and XPS results confirm that substitutional doping of Zr in the ceria crystal lattice, i.e., the formation of a solid solution, occurs for all of the doped samples. Furthermore, zirconium-doped samples show superior thermal stability compared to the undoped sample. The 10 mol. % zirconium doped sample has the best overall properties, notably the best catalytic activity in the BTEX oxidation process, exhibiting the lowest 90% conversion temperatures for all analyzed volatile organic compounds.

Author Contributions: Conceptualization, K.M. and S.K.; methodology, K.M. and S.K.; formal analysis, K.M., S.K., H.B.-R., F.B. and M.D.; writing—original draft preparation, K.M.; writing—review and editing, K.M., S.K., H.B.-R., F.B. and M.D.; visualization, K.M., H.B.-R. and F.B.; supervision, S.K.; project administration, S.K.; funding acquisition, S.K. All authors have read and agreed to the published version of the manuscript.

Funding: This work has been fully supported by Croatian Science Foundation under the project IP-01-2018-2963.

Data Availability Statement: The original contributions presented in the study are included in the article, further inquiries can be directed to the corresponding author.

Acknowledgments: The support of the University of Zagreb and the University of Rijeka is gratefully acknowledged.

Conflicts of Interest: The authors declare no conflicts of interest.

References

- 1. Zafar, M.; Mahmood, S.; Shaikh, H.; Alhamidi, A.; Ramay, S.M.; Saleem, M.; Siddiqi, S.A. Structural, dielectric and optical investigations of Zr incorporated ceria nanoparticles. *Mater. Res. Express* **2019**, 2, 116321. [CrossRef]
- Sahoo, S.K.; Mohapatra, M.; Anand, S. Absorption and emission properties of Zr-doped nanoceria synthesised by co-precipitation-hydrothermal treatment route. J. Exp. Nanosci. 2015, 10, 1012–1027. [CrossRef]
- 3. Joseph, A.; Mathew, K.P.J.; Vandana, S. Zirconium-Doped Ceria Nanoparticles as Anticorrosion Pigments in Waterborne Epoxy–Polymer Coatings. *ACS Appl. Nano Mater.* **2021**, *4*, 834–849. [CrossRef]
- Ghosh, S.; Thomas, T.; Rao, G.R. Zr substitution aided enhancement of pseudocapacitive behavior of ceria. Mater. Lett. 2020, 266, 127500. [CrossRef]

5. Moos, R.; Izu, N.; Rettig, F.; Reiß, S.; Shin, W.; Matsubara, I. Resistive Oxygen Gas Sensors for Harsh Environments. *Sensors* **2011**, 11, 3439–3465. [CrossRef] [PubMed]

- Gutiérrez-Ortiz, J.I.; De Rivas, B.; López-Fonseca, R.; González-Velasco, J.R. Combustion of aliphatic C₂ chlorohydrocarbons over ceria–zirconia mixed oxides catalysts. *Appl. Catal. A Gen.* 2004, 269, 147–155. [CrossRef]
- Li, L.; Li, P.; Wang, Y.; Lin, L.; Shah, A.H.; He, T. Modulation of oxygen vacancy in hydrangea-like ceria via Zr doping for CO₂ photoreduction. *Appl. Surf. Sci.* 2018, 452, 498–506. [CrossRef]
- 8. Rizzuti, A.; Dipalo, M.C.; Allegretta, I.; Terzano, R.; Cioffi, N.; Mastrorilli, P.; Mali, M.; Romanazzi, G.; Nacci, A.; Dell'Anna, M.M. Microwave-Assisted Solvothermal Synthesis of Fe₃O₄/CeO₂ Nanocomposites and Their Catalytic Activity in the Imine Formation from Benzyl Alcohol and Aniline. *Catalysts* **2020**, *10*, 1325. [CrossRef]
- 9. Trovarelli, A. Catalytic Properties of Ceria and CeO₂-Containing Materials. Catal. Rev. Sci. Eng. 1996, 38, 439–520. [CrossRef]
- 10. Trovarelli, A.; Fornasiero, P. (Eds.) *Catalysis by Ceria and Related Materials*, 2nd ed.; Catalytic Science Series; Imperial College Press: London, UK, 2013; Volume 12.
- 11. Montini, T.; Melchionna, M.; Monai, M.; Fornasiero, P. Fundamentals and catalytic applications of CeO₂-based materials. *Chem. Rev.* **2016**, *116*, 5987–6041. [CrossRef]
- 12. Huang, H.; Xu, Y.; Feng, Q.; Leung, D.Y.C. Low temperature catalytic oxidation of volatile organic compounds: A review. *Catal. Sci. Technol.* **2015**, *5*, 2649–2669. [CrossRef]
- 13. Dhall, A.; Self, W. Cerium Oxide Nanoparticles: A Brief Review of Their Synthesis Methods and Biomedical Applications. *Antioxidants* **2018**, *7*, 97. [CrossRef]
- 14. Stojanovic, B.D.; Dzunuzovic, A.S.; Ilic, N.I. Review of methods for the preparation of magnetic metal oxides. In *Magnetic, Ferroelectric, and Multiferroic Metal Oxides*; Stojanovic, B.D., Ed.; Elsevier: Amsterdam, The Netherlands, 2018; pp. 333–359. [CrossRef]
- 15. Mandić, V.; Kurajica, S.; Mužina, K.; Brleković, F.; Munda, I.K. Tailoring thermal development of gamma alumina sorbents material using combustion synthesis: The effect of amino acids (G, A, N) and equivalence ratio. *J. Therm. Anal. Calorim.* **2020**, 142, 1681–1691. [CrossRef]
- 16. Kurajica, S.; Mandić, V.; Mužina, K.; Panžić, I.; Kralj, D.; Duplančić, M.; Ivković, I.K. Thermal stability and properties of Pd/CeAlO₃ catalyst prepared by combustion synthesis. *J. Therm. Anal. Calorim.* **2023**, *148*, 10481–10490. [CrossRef]
- 17. Mužina, K.; Kurajica, S.; Guggenberger, P.; Duplančić, M.; Dražić, G. Catalytic activity and properties of copper-doped ceria nanocatalyst for VOCs oxidation. *J. Mater. Res.* **2022**, *37*, 1929–1940. [CrossRef]
- 18. Kurajica, S.; Mužina, K.; Dražić, G.; Matijašić, G.; Duplančić, M.; Mandić, V.; Župančić, M.; Munda, I.K. A comparative study of hydrothermally derived Mn, Fe, Co, Ni, Cu and Zn doped ceria nanocatalysts. *Mater. Chem. Phys.* **2020**, 244, 122689. [CrossRef]
- 19. López, R.; Gómez, R. Band-gap energy estimation from diffuse reflectance measurements on sol–gel and commercial TiO₂: A comparative study. *J. Sol-Gel Sci. Technol.* **2012**, *61*, 1–7. [CrossRef]
- 20. Denton, A.R.; Ashcroft, N.W. Vegard's law. *Phys. Rev. A* **1991**, 43, 3161–3164. [CrossRef]
- Roque-Ruiz, J.H.; Reyes-López, S.Y. Synthesis of α-Al₂O₃ Nanopowders at Low Temperature from Aluminum Formate by Combustion Process. J. Mater. Sci. Eng. 2016, 6, 1000305. [CrossRef]
- 22. Lin, C.P.; Wen, S.B. Variations in a Boehmite Gel and Oleic Acid Emulsion under Calcination. *J. Am. Ceram. Soc.* **2002**, *85*, 1467–1472. [CrossRef]
- 23. Abo-almaged, H.H.; Khattab, R.M.; Sadek, H.E. Preparation and characterization of ZrO₂/CeO₂ ceramic composite synthesized by microwave combustion method. *Orient. J. Chem.* **2016**, *32*, 243. [CrossRef]
- 24. Venancio, S.A.; de Miranda, P.E.V. Synthesis of CeAlO₃/CeO₂-Al₂O₃ for use as a solid oxide fuell cell functional anode material. *Ceram. Int.* **2011**, *37*, 3139–3152. [CrossRef]
- 25. Nhiem, D.N.; Dai, L.M.; Van, N.D.; Lim, D.T. Catalytic oxidation of carbon monoxide over nanostructured CeO₂-Al₂O₃ prepared by combustion method using polyvinyl alcohol. *Ceram. Int.* **2013**, *39*, 3381–3385. [CrossRef]
- Cassel, R.B. Determining Volatiles in Polyethylene Terephthalate Using the Q5000 IR Thermogravimetric Analyzer, TA326, TA
 Instruments. Available online: https://www.tainstruments.com/pdf/literature/TA326.pdf (accessed on 4 July 2023).
- 27. Kumar, E.; Selvarajan, P.; Muthuraj, D. Synthesis and Characterization of CeO₂ Nanocrystals by Solvothermal Route. *Mater. Res.* **2013**, *16*, 269–276. [CrossRef]
- 28. Nadjia, L.; Abdelkader, E.; Naceur, B.; Ahmed, B. CeO₂ nanoscale particles: Synthesis, characterization and photocatalytic activity under UVA light irradiation. *J. Rare Earths* **2018**, *36*, 575–587. [CrossRef]
- 29. Choudhury, B.; Chetri, P.; Choudhury, A. Oxygen defects and formation of Ce³⁺ affecting the photocatalytic performance of CeO₂ nanoparticles. *RSC Adv.* **2014**, *4*, 4663–4671. [CrossRef]
- 30. Pop, O.L.; Mesaros, A.; Vodnar, D.C.; Suharoschi, R.; Tabaran, F.; Magerusan, L.; Todor, I.S.; Diaconeasa, Z.; Balint, A.; Ciontea, L.; et al. Cerium oxide nanoparticles and their efficient antibacterial application in vitro against gram-positive and gram-negative pathogens. *Nanomaterials* **2020**, *10*, 1614. [CrossRef]
- 31. Sharan, R.; Dutta, A. Structural analysis of Zr⁴⁺ doped ceria, a possible material for ammonia detection in ppm level. *J. Alloys Compd.* **2017**, 693, 936–944. [CrossRef]
- 32. Venkataswamy, P.; Rao, K.N.; Jampaiah, D.; Reddy, B.M. Nanostructured manganese doped ceria solid solutions for CO oxidation at lower temperatures. *Appl. Catal. B Environ.* **2015**, *162*, 122–132. [CrossRef]

33. Garcia, X.; Soler, L.; Divins, N.J.; Vendrell, X.; Serrano, I.; Lucentini, I.; Prat, J.; Solano, E.; Tallarida, M.; Escudero, C.; et al. Ceria-based catalysts studied by near ambient pressure X-ray photoelectron spectroscopy: A review. *Catalysts* **2020**, *10*, 286. [CrossRef]

- 34. Tu, Y.; Chen, S.; Li, X.; Gorbaciova, J.; Gillin, W.P.; Krause, S.; Briscoe, J. Control of oxygen vacancies in ZnO nanorods by annealing and their influence on ZnO/PEDOT:PSS diode behaviour. *J. Mater. Chem. C* **2018**, *6*, 1815–1821. [CrossRef]
- 35. Aranda, A.; Agouram, S.; López, J.M.; Mastral, A.M.; Sellick, D.R.; Solsona, B.; Taylor, S.H.; García, T. Oxygen defects: The key parameter controlling the activity and selectivity of mesoporous copper-doped ceria for the total oxidation of naphthalene. *Appl. Catal. B Environ.* **2012**, 127, 77–88. [CrossRef]
- Kumar, P.S.V.; Suresh, L.; Vinodkumar, T.; Reddy, B.M.; Chandramouli, G.V.P. Zirconium Doped Ceria Nanoparticles: An Efficient and Reusable Catalyst for a Green Multicomponent Synthesis of Novel Phenyldiazenyl–Chromene Derivatives Using Aqueous Medium. ACS Sustain. Chem. Eng. 2016, 4, 2376–2386. [CrossRef]
- Koleva, I.Z.; Aleksandrov, H.A.; Neyman, K.M.; Vayssilov, G.N. Preferential location of zirconium dopants in cerium dioxide nanoparticles and the effects of doping on their reducibility: A DFT study. Phys. Chem. Chem. Phys. 2020, 22, 26568–26582.
 ICrossRefl
- 38. Vári, G.; Óvári, L.; Papp, C.; Steinrück, H.-P.; Kiss, J.; Kónya, Z. The Interaction of Cobalt with CeO₂(111) Prepared on Cu(111). *J. Phys. Chem. C* **2015**, *119*, 9324–9333. [CrossRef]
- 39. Thommes, M.; Kaneko, K.; Neimark, A.V.; Olivier, J.P.; Rodriguez-Reinoso, F.; Rouquerol, J.; Sing, K.S.W. Physisorption of gases, with special reference to the evaluation of surface area and pore size distribution (IUPAC Technical Report). *Pure Appl. Chem.* **2015**, *87*, 1051–1069. [CrossRef]
- 40. Sotomayor, F.J.; Cychosz, K.A.; Thommes, M. Characterization of micro/mesoporous materials by physisorption: Concepts and case studies. *Acc. Mater. Surf. Res.* **2018**, *3*, 34–50.
- 41. Varma, A.; Mukasyan, A.S.; Rogachev, A.S.; Manukyan, K.V. Solution Combustion Synthesis of Nanoscale Materials. *Chem. Rev.* **2016**, *116*, 14493–14586. [CrossRef]
- 42. Bernard, P.; Stelmachowski, P.; Bros, P.; Makowski, W.; Kotarba, A. Demonstration of the Influence of Specific Surface Area on Reaction Rate in Heterogeneous Catalysis. *J. Chem. Educ.* **2021**, *98*, 935–940. [CrossRef]
- 43. Zhou, G.; Lan, H.; Song, R.; Xie, H. Effects of preparation method on CeCu oxide catalyst performance. *RSC Adv.* **2014**, *4*, 50840–50850. [CrossRef]
- 44. Liu, S.; Wu, X.; Weng, D.; Ran, R. Ceria-based catalysts for soot oxidation: A review. J. Rare Earths 2015, 33, 567–590. [CrossRef]
- 45. Ramos-Fernandez, E.V.; Shiju, N.R.; Rothenberg, G. Understanding the solar-driven reduction of CO₂ on doped ceria. *RSC Adv.* **2014**, *4*, 16456–16463. [CrossRef]

Disclaimer/Publisher's Note: The statements, opinions and data contained in all publications are solely those of the individual author(s) and contributor(s) and not of MDPI and/or the editor(s). MDPI and/or the editor(s) disclaim responsibility for any injury to people or property resulting from any ideas, methods, instructions or products referred to in the content.